Chemical Geology 291 (2012) 175–185

Contents lists available at SciVerse ScienceDirect

Chemical Geology

journal homepage: www.elsevier.com/locate/chemgeo

Research papers

Measurement of ^{7}Be in soils and sediments by gamma spectroscopy

Joshua D. Landis [a,*], Carl E. Renshaw [a], James M. Kaste [b]

[a] Department of Earth Sciences, Dartmouth College, Hanover, NH 03755, USA
[b] Department of Geology, College of William and Mary, Williamsburg, VA 23187, USA

ARTICLE INFO

Article history:
Received 8 June 2011
Received in revised form 5 October 2011
Accepted 11 October 2011
Available online 20 October 2011

Editor: J.D. Blum

Keywords:
Beryllium-7
Gamma
Interference
Integration
Precision
Actinium-228

ABSTRACT

Measurement of cosmogenic ^{7}Be in soils and sediments by gamma spectroscopy has been routine for three decades. However, the analytical constraints of this method have yet to be adequately described. Natural abundance of ^{7}Be in bulk soils and sediments is typically low (10^{6} to 10^{8} atoms kg^{-1}), resulting in very low signal-to-noise ratio in the gamma spectrum. ^{7}Be quantification is further complicated by numerous interferences from ubiquitous ^{238}U- and ^{232}Th-series radionuclides. We investigated the environmental gamma spectrum in the region of ^{7}Be emission using spectra obtained from hundreds of natural stream sediment samples, one well-characterized sediment naturally-enriched in ^{7}Be, and pure standard materials enriched in both ^{238}U-series and ^{232}Th-series decay chains. In typical samples no fewer than three discrete photopeaks directly interfere with ^{7}Be measurement, one of which, the ^{228}Ac 478.3 keV photon, yields significant positive bias. Risks of ^{7}Be false-positives due to this overlapping photopeak approach 50% for typical soils or sediments. Detection limits for ^{7}Be in these materials using conventional high-purity germanium instruments are as low as 0.1 Bq, but increase by up to a factor of four in the presence of modest activities of ^{238}U- and ^{232}Th-series nuclides. Here we demonstrate a methodology for the measurement of low ^{7}Be abundances in soils and sediments that is unbiased and that optimizes precision.

1. Introduction

Environmental scientists increasingly recognize beryllium-7 as a valuable tracer of soil and sediment dynamics. Growing interest in ^{7}Be derives from its atmospheric origin, global distribution and continuous delivery to Earth's surface; its acute particle reactivity, which results in rapid, irreversible "tagging" of surface materials; its half-life (~53.3 d), which captures the timescale of many active sediment and particulate contaminant transport processes; and from the relative ease of acquiring ^{7}Be measurements by gamma spectroscopy (see review in Kaste et al., 2002). Recent geomorphological applications of this natural tracer include: quantifying erosion (Wallbrink and Murray, 1993; Wilson et al., 2003; Blake et al., 2009; Walling et al., 2009); identifying sediment sources (Walling and Woodward, 1992; Whiting et al., 2005); quantifying sediment deposition (Olsen et al., 1986) and dating of depositional events (Matisoff et al., 2005; Fisher et al., 2010), tracking of discrete sediment packages during mobilization (Salant et al., 2006); sediment mobilization and coupled contaminant fate (Fitzgerald et al., 2001; Saari et al., 2010); erosional remediation (Schuller et al., 2010); coupled trace-metal dynamics during soil organic matter decomposition (Kaste et al., 2011); and quantifying floodplain age and river migration rates (Black et al., 2010). With respect to ^{7}Be analytical methodology, these authors typically forego detailed discussion and/or cite Larsen and Cutshall (1981), who first described simple in situ (i.e., without chemical separation) measurement of ^{7}Be in enriched sediments.

But typical ^{7}Be soil steady-state inventories are very low globally, in the range of 0.02 to 0.1 becquerels (Bq) per cm^{2} (Dibb, 1989; Todd et al., 1989; Wallbrink and Murray, 1994; Zhu and Olsen, 2009), amounting to just 10^{-18} g ^{7}Be per gram soil disseminated in the uppermost 2 cm of the Earth surface. Equivalent soil abundances are <30 Bq/kg. In fluvial systems, transport, mixing and decay quickly dilute ^{7}Be to near the detection limits of typical gamma spectrometers, which are on the order of 1 Bq/kg for conventional high-purity germanium (HPGe) detector and shield systems and 1 to 2 day count times. Contemporary improvements in HPGe detector characteristics, while having bettered low-level measurements, also reveal spectral features that impinge on the direct measure of ^{7}Be at 477.6 keV. One photopeak in particular, derived from the ubiquitous thorium-232 granddaughter actiniun-228, is not resolvable from the ^{7}Be peak. Here we characterize the environmental ^{7}Be photoregion, demonstrating the complexity of gamma emissions in the 450–500 keV range, and showing "average" contributions of low-abundance photopeaks to real soil and sediment samples via a composite spectrum. For the case of singular measurements, we evaluate true risks to ^{7}Be detection and quantitation using well-accepted detection criteria and Poisson-based numerical models. We then introduce an experimental design that demonstrates a methodology for the accurate and precise integration of ^{7}Be in soil and sediment samples with varying degrees of spectral interference.

* Corresponding author. Tel.: +1 603 646 6564.
E-mail address: jlandis@dartmouth.edu (J.D. Landis).

0009-2541/$ – see front matter © 2011 Elsevier B.V. All rights reserved.
doi:10.1016/j.chemgeo.2011.10.007

2. Background

Beryllium-7 is measurable by gamma spectroscopy via its single photo-emission at 477.6035 keV (10.44% yield; Chu et al., 1999). Given the limitations of ^{7}Be measurement by accelerator mass spectrometry (Raisbeck and Yiou, 1988; Nagai et al., 2004), gamma counting remains the only routine method for measuring this natural radionuclide. Low ^{7}Be abundances in natural soils and sediments force the adoption of gamma counting procedures that optimize instrument sensitivity, so-called large-volume, close-in geometry. Unfortunately, these conditions simultaneously favor the detection of numerous interfering photopeaks derived from both ^{238}U- and ^{232}Th-series nuclides. Despite having very low nuclear yields, these interferences are detectable, produce background excursions in the region immediately surrounding the ^{7}Be peak, and preclude the designation of true background regions immediately adjacent to the ^{7}Be peak. Moreover, ^{7}Be suffers convolution with the 478.3 keV photoemission of ^{228}Ac (0.21% yield; Helmer, 1979; Chu et al., 1999). This interference is not resolvable with conventional HPGe detectors, whose peak width (σ_G) at this energy is typically on the order of 0.5 keV or ~1.2 keV full-width at half-maximum (FWHM). Despite its very low yield, the interfering ^{228}Ac photopeak is readily detected in soils and sediments using normal HPGe detectors, standard shielding, and common count durations. If unaccounted for, the ^{228}Ac interference significantly biases measurement of ^{7}Be abundances.

Actinium-228 (half-life 6.2 h) is a short-lived granddaughter of ubiquitous ^{232}Th. As a consequence of its very short half-life, ^{228}Ac activity is supported in natural materials by secular equilibrium with its immediate parent ^{228}Ra (half-life 5.75 a), which in turn is supported by primordial ^{232}Th (half-life 10^{14} a). Decay of ^{228}Ac yields gamma photons at more than 200 discrete energy levels (Helmer, 1979; Dalmasso et al., 1984, 1987), making it one of the foremost single contributors of complexity in the environmental gamma spectrum. Using any one of its several high-yield photopeaks, especially 911.2 keV (yield 25.8%), abundance of ^{228}Ac in environmental samples is measurable to better than 1% relative. Predicting the contribution of the ^{228}Ac 478.3 keV photon to a ^{7}Be photopeak is then possible with good precision (typically <5% relative):

$$R^{\mathrm{Ac-228}}_{478\,\mathrm{keV}} = R^{\mathrm{Ac-228}}_{911\,\mathrm{keV}} \cdot \frac{\gamma^{\mathrm{Ac-228}}_{478\,\mathrm{keV}}}{\gamma^{\mathrm{Ac-228}}_{911\,\mathrm{keV}}} \cdot \frac{\varepsilon^{\mathrm{Ac-228}}_{478\,\mathrm{keV}}}{\varepsilon^{\mathrm{Ac-228}}_{911\,\mathrm{keV}}} \quad (1)$$

where R is spectrum count rate [counts per second] of the indicated photopeak, γ is nuclear decay yield or branching ratio of the specified photon, and ε is net efficiency of the gamma detector at the specified energy. As in classical arithmetic deconvolution, the ^{228}Ac contribution may then be subtracted from the combined area of the ^{7}Be–^{228}Ac doublet to estimate the true ^{7}Be peak area. The nominal bias we predict by this approach amounts to ~16 mBq false contribution to ^{7}Be for each 1 Bq ^{228}Ac in the sample, or ~0.5 Bq/kg bias in ^{7}Be for a typical sediment sample which contains 30 Bq/kg ^{228}Ac.

But removing the ^{7}Be interference is not so simple in real samples. Because net count rates of both ^{7}Be and ^{228}Ac 478 keV peaks are often very low, neither is full-width resolved in a typical sediment sample HPGe spectrum, meaning that the observed, detectable signal of each peak will be some fraction of their true full-width area. Furthermore, the actual count rate we observe for the ^{228}Ac interferent varies from nominal prediction due to Poisson uncertainty (where anticipated peak area is $N \pm \sqrt{N}$ counts), which may introduce a large uncertainty during ^{7}Be deconvolution. These circumstances demand careful assessment of quantitation methods, and ultimately dictate a refined approach if we wish to fully exploit ^{7}Be as a tracer of soil and sediment dynamics.

3. Low-abundance photopeaks and limits of detection

Nuclides of the ^{238}U and ^{232}Th decay series are globally ubiquitous in soils and sediments, locally homogeneous by virtue of their lithologic origin, and generally conservative during chemical weathering of the Earth near-surface (e.g., Gascoyne, 1992; Chabaux et al., 2003). Consequently, they make comparable contributions to the gamma spectrum of geogenic materials in a given locality, and we expect that summing many sample spectra into a single composite will overcome the statistical limitations of any one sample measurement. In Fig. 1 we present a weighted composite spectrum of 400 ^{7}Be-free sediments from the upper Connecticut River valley region in central Vermont (VT) and New Hampshire (NH), USA. Details on spectrum collection are given later in Section 4, but here we note our use of normal HPGe detectors and shielding without low-background equipment or Compton-suppression. Sample sediments were packed in 84×20 mm polyethylene cups and placed directly on the detector endcap.

Our composite spectrum shows a clear and strong maximum, offset from the ^{7}Be centroid energy and corresponding to the ^{228}Ac 478.3 keV photon. Numerous other low-yield features are attributable to photopeaks of ^{212}Bi at 453 keV; ^{214}Bi at 455, 470 and 474 keV; ^{214}Pb at 462, 480 and 487 keV (Table 1). Conversely, the energies 458–459.5 and 482.5–485 keV appear free from spectral features and we therefore take them to give true estimates of background. Variation through and between these regions-of-interest (ROI) is broadly linear, implying that a linear background model is appropriate for estimating background continuum contributions to the ^{7}Be photopeak. In the discussion and analyses to follow all ^{7}Be integrations use this background definition.

Interpretation of features in the composite spectrum is based on nuclear data compiled by Chu et al. (1999) and summarized in Table 1. Using these data, the hypothetical photopeak count rate for a nuclide of activity concentration A within a specified detector channel i is predictable by

$$R_i = A \cdot \gamma \cdot \varepsilon \cdot m \cdot p_i \quad (2)$$

where R_i is count rate [counts per second], A is activity concentration [Bq/kg], γ is photon emission yield, ε is detector net efficiency, and m is sample mass [kg]. The term p_i is the normalized emission probability density of a given photopeak over the specified channel or range of channels, i.e., the fraction of total peak area integrated within the specified channel(s). Gamma peaks are nearly Gaussian in shape, with subtle tailing near baseline at the low-energy side and perhaps at high-energy side, as well. Here these tails are modeled as exponential functions, and the peak shape model for the estimation of p_i may be written as

$$p_i = p(x_i) = \left[\int_{-\infty}^{L} e^{\frac{L\cdot(2x-2\mu+L)}{2\sigma^2}} + \int_{L}^{H} e^{\frac{-(x-\mu)^2}{2\sigma^2}} + \int_{H}^{\infty} e^{\frac{H\cdot(2\cdot\mu-2x+H)}{2\sigma^2}} \right] \div \int_{-\infty}^{+\infty} p(x_i) \quad (3)$$

where x_i is channel energy [kev]; σ_G is Gaussian peak width [keV]; μ is peak centroid position [keV], L is the distance from centroid at which tailing begins at the low energy side [keV], and H at the high energy side [keV]. The count rate R_i in each channel of a photopeak (Eq. (2)) may be predicted or modeled as the product of peak height, represented with h, and probability density, p_i. Least-squares fitting between our composite and a model spectrum predicted using Eqs. (2) and (3) yields U-series and Th-series activities consistent with values for these samples measured independently via nuclides ^{214}Pb (median 19.7 Bq/kg) and ^{228}Ac (median 25.4 Bq/kg); these values are typical for fluvial sediments and approximate the average crustal U:Th activity ratio.

Measurement of ^{7}Be also suffers a secondary, non-specific interference that is evident from our preceding analysis: background

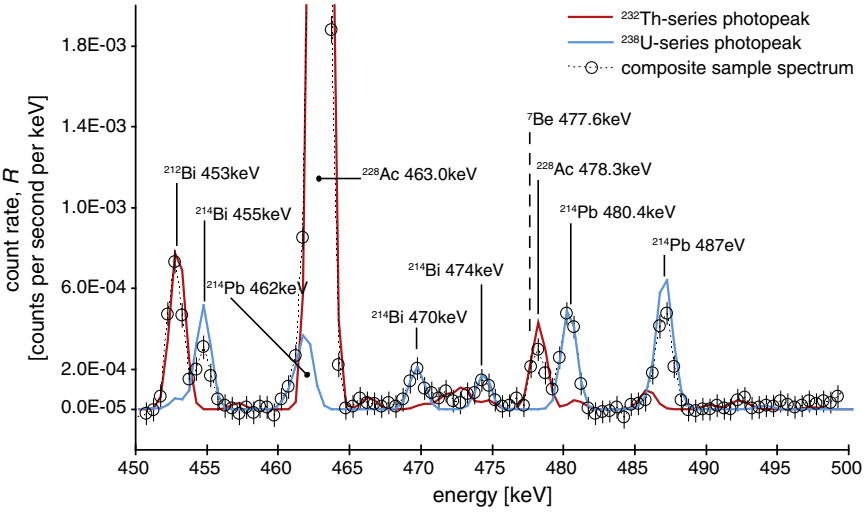

Fig. 1. Beryllium-7 photoregion for fluvial sediments, showing emissions of the ^{238}U and ^{232}Th decay series. Open circles show a variance-weighted composite spectrum of 400 ^{7}Be-free sediments. Nominal position of the ^{7}Be photopeak is shown for comparison, though no ^{7}Be is present. Solid lines are best-fits to each natural decay series based on published nuclear data (Chu et al., 1999). Observed peaks smaller than prediction (455 keV, 478 keV, 487 keV) reflect coincidence-summing losses from cascade-emitting nuclides ^{214}Bi, ^{228}Ac, and ^{214}Pb, respectively.

height in a sample spectrum increases in proportion to the total amount of ^{228}Ac in a sample (adj $R^2 = 0.79$, $P < 2.2 \times 10^{-16}$). Background height impacts ^{7}Be measurements, since background *uncertainty* increases as the square root of background height ($\sigma_N = \sqrt{N}$) and directly determines detection limits (Currie, 1968). The increase in background contributions is attributable to cumulative Compton scattering throughout the gamma spectrum and not specifically to ^{228}Ac or any other single peak or nuclide — we find that ^{228}Ac activity is simply a reasonable estimator of gross radionuclide abundance in sediments, a consequence of common mineral origins and similarly conservative nature of the ^{238}U- and ^{232}Th-series nuclides.

Using well-established detection criteria (Currie, 1968), we evaluate the relevance of background height to individual measurements of ^{228}Ac and ^{7}Be photopeaks at 478 keV. Fig. 2 presents limits of detection for our 400 representative spectra, as well as generalized predictions based on background count rates predicted from in situ ^{228}Ac activity. For comparison, Fig. 2a also shows typical ^{228}Ac count rates expected for global soils (UNSCEAR, 2000) via Eq. (2). Details of these analyses are described in the Appendix A. Fig. 2a shows that the ^{228}Ac 478 keV photon is detectable, i.e. resolved from background, in *typical* soil and sediment HPGe spectra with 50% probability in 1.1 days, with 10% probability in 0.6 days, and with 1% probability in 0.3 days. Higher amounts of ^{228}Ac are detectable in shorter count times. To be clear, insofar as the ^{7}Be and ^{228}Ac peaks are poorly resolved, these probabilities are risks of ^{7}Be false positives in excess of those we expect due to background continuum alone.

Beryllium-7 detection limits are displayed in Fig. 2b as the minimum-detectable-activity (MDA) or concentration (MDC), the

Table 1
Gamma emissions in the ^{7}Be photoregion (450–500 keV) for environmental HPGe spectra.

Nuclide	Source	Centroid (keV)	*s*	Yield	*s*	Detection[1] (days)	Reference
^{228}Ac	^{232}Th	452.47	0.01	0.015%	0.0005%	93	a
^{214}Bi	^{238}U	452.92	0.1	0.031%	0.004%	13	a
^{212}Bi	^{232}Th	452.98	0.05	0.363%	0.003%	0.02	a
^{214}Bi	^{238}U	454.77	0.12	0.30%	0.02%	0.02	a
^{228}Ac	^{232}Th	457.17	0.15	0.015%	0.002%	95	a
^{214}Bi	^{238}U	461.0	0.2	0.053%	0.009%	4	a
^{214}Pb	^{238}U	462.00	0.07	0.221%	0.009%	0.07	a
^{228}Ac	^{232}Th	463.000	0.006	4.4%	0.2%	0.004	a,b,c
^{228}Ac	^{232}Th	466.4	0.1	0.030%	0.0003%	23	a
^{214}Bi	^{238}U	469.76	0.07	0.13%	0.01%	0.4	a
^{228}Ac	^{232}Th	470.25	0.2	0.0133%	0.0003%	137	a
^{228}Ac	^{232}Th	471.76	0.15	0.0336%	0.0003%	17	a
^{212}Bi	^{232}Th	473.0	0.7	0.050%	0.004%	7	a
^{214}Bi	^{238}U	474.41	0.05	0.110%	0.009%	1	a
^{228}Ac	^{232}Th	474.75	0.1	0.023%	0.0003%	44	a
^{7}Be	cosmogenic	477.604	0.002	10.44%	0.04%	n/a	a
^{228}Ac	^{232}Th	478.33	0.011	0.21%	0.02%	0.2	a,b,c
^{214}Pb	^{238}U	480.43	0.02	0.32%	0.01%	0.02	a
^{228}Ac	^{232}Th	480.94	0.2	0.0230%	0.0005%	41	a
^{214}Pb	^{238}U	487.09	0.07	0.42%	0.02%	0.004	a
^{214}Bi	^{238}U	487.95	0.13	0.028%	0.009%	19	a
^{228}Ac	^{232}Th	490.33	0.15	0.012%	0.003%	207	b
^{228}Ac	^{232}Th	492.37	0.01	0.026%	0.003%	41	b
^{214}Bi	^{238}U	494.2	0.4	0.012%	0.003%	127	a

a, Chu et al. (1999); b, Dalmasso et al. (1987); c, Helmer (1979).
[1] Estimated count time, in days, for a peak to exceed the Currie (1968) critical limit, i.e. to be resolved from background ($k_1 = k_2 = 1.645$, $\alpha = \beta = 5\%$; see Appendix A).

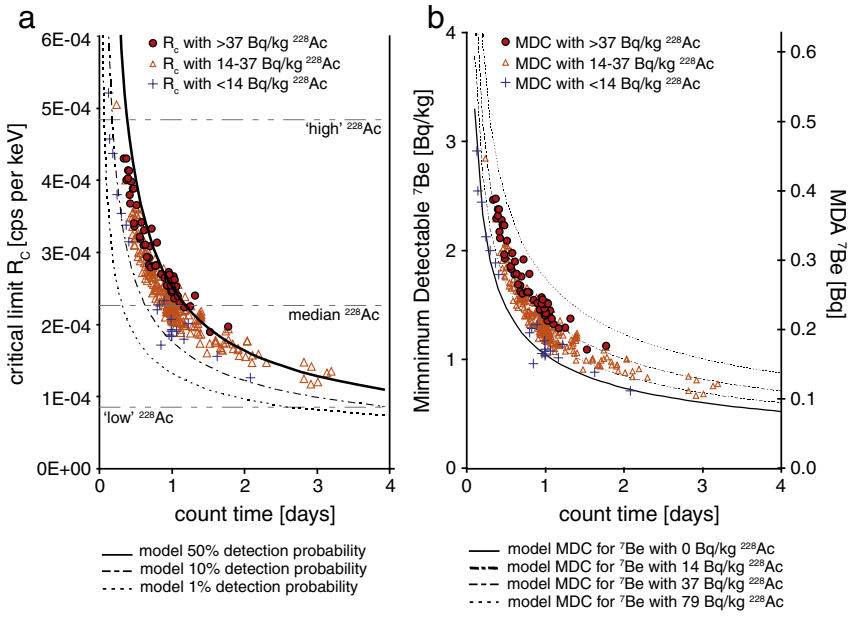

Fig. 2. a, Data points show Currie (1968) critical limit at 478 keV, i.e. maximum likely background count rate with specified probability ($\alpha = 5\%$). Points are marked by total ^{228}Ac measured in each sample. Curved lines show the count time at which the ^{228}Ac 478 keV photon will exceed critical limit with the specified probability (50%, 10% or 1%) and therefore impinge on ^{7}Be detection and quantitation. Global soil ^{228}Ac count rates (UNSCEAR, 2000) are shown for comparison as horizontal lines, indicating for example that the median soil ^{228}Ac activity is detectable with 50% probability in 1.1 days (see Appendix A). b, Detection limits as minimum concentration (MDC) and activity (MDA) for ^{7}Be for same spectra, where detection limit assesses both false-positive ($\alpha = 5\%$) and false-negative ($\beta = 5\%$). Curved lines show detection limit increasing proportional to in situ ^{228}Ac.

lowest ^{7}Be activity that we can measure reliably with just 5% probability of false-negative. These limits are a function of count time and also of total ^{228}Ac in the sample: the former due to counting statistics, the latter a result both of background enhancement and of direct overlap with the 478 keV photopeak. In soils and sediments the ^{7}Be MDC is ~1.0 Bq/kg for 1-day counts, increasing by a factor of 2 in the presence of high ^{228}Ac activities. The minimum ^{7}Be concentrations resolvable from background (i.e., critical limit) are a factor of two less than this or ~0.5 Bq/kg for a 1-day count.

4. Unbiased ^{7}Be measurement

4.1. Experimental design

Having demonstrated the complexity of the ^{7}Be photoregion, and that ^{228}Ac interference is likely in typical HPGe measurements of ^{7}Be in soils and sediments, we now describe an experimental design that demonstrates the sensitivity of different analytical methods to these sources of bias. For this experiment, we collected a quantity of silty overbank stream sediment naturally enriched in ^{7}Be. The sediment was dried, pulverized, homogenized, divided and then spiked with environmentally-relevant amounts of ^{228}Ac. In the non-spiked sample, ^{238}U- and ^{232}Th-series radionuclide concentrations are close to both local and global median values, 28.87 ± 0.38 Bq/kg ^{226}Ra and 29.93 ± 0.12 Bq/kg ^{228}Ac (mean $\pm$ 2SE). Thorium-ore OKA-2 (CCMRP, Natural Resource Canada, Ottawa, Ontario) was added as a spike at levels 1.5×, 2×, 3× and 5× the in situ ^{228}Ac. The resulting range of ^{228}Ac concentration in our sample suite is 30–150 Bq/kg. Only modest amounts of ^{238}U and ^{235}U nuclides are present in the spike, amounting to an additional 8% added in the highest spike level.

All samples were packed into puck-shaped 84×20 mm (ca. 110 cm^3) polyethylene cups and measured via HPGe gamma spectroscopy 23–27 times each over a period of 8 months (4.5 half-lives). Samples are placed directly on the detector endcap, situating their lower surface ca. 6.5 mm from the detector crystal. Count time for each measurement was 4 days, and samples were rotated among four p-type germanium detectors (Canberra model number BEGe3830). The BEGe 3830 crystal is an HPGe planar-type cylinder of 70 mm diameter and 30 mm thickness. Each detector is housed in conventional shielding, consisting of 4 in. of low-background lead with graded tin and copper lining and a 10 mm steel jacket. Data acquisition is performed via a commercial system consisting of an analog preamplifier (Canberra model 2002CSL) incorporated in the detector cryostat and coupled to a digital multi-channel analyzer (Canberra model DSA1000). For these detectors resolution at 478 keV is $\sigma_G = 0.5$ keV or 1.2 FWHM; net efficiency at this energy is ca. 3.2%; peak-to-Compton ratios are approximately 57:1; and background count rates at 478 keV are ca. 54 counts per day per keV. As demonstrated shortly, we determined ^{7}Be concentration of the test material to be 12.25 ± 0.30 Bq/kg (variance-weighted average $\pm$ 2SE; $n = 120$). In the absence of an affordable ^{7}Be standard material, we used the natural decay of ^{7}Be at a known rate (0.0130 d^{-1}) to standardize subsequent re-measurement at extended half-lives. This approach provides us with numerous "virtual" standards of identical composition but variable ^{7}Be concentration and ^{7}Be:^{228}Ac peak-area ratios.

4.2. Detector calibration

4.2.1. Net efficiency calibration

Net detector efficiency is a simple ratio, the number of counts per second *observed* for a given photon versus the number of decays per second (activity) known to exist in the emitting material:

$$\varepsilon = \frac{R^*}{A^* \cdot m^* \cdot \gamma \cdot p} \tag{4}$$

where ε is net efficiency, R^* is measured count rate in the spectrum of the given photon emitted by the calibration material, A^* is certified activity concentration of the reference ore, m^* is mass of the ore spike, and p is the normalized probability density of the photopeak as described in Eqs. (2) and (3). The term p is included here as a provision for cases where low-yield photons and/or low activity standards are used for calibration, because their photopeaks may not be full-width resolved from background over common count durations. We calibrate our gamma detectors using test and other representative materials

spiked with either uranium or thorium reference ore (U-ore BL5, Th-ore OKA2, both CCRMP). Ore additions are made at ≤1 wt.%, a tradeoff between improving counting statistics (shortening count times) and degrading photon attenuation due to the high heavy-element content of the ores. Both materials are reported to be in secular equilibrium (Faye et al., 1979; Smith et al., 1986; Oddone et al., 2008). We derive efficiency for the ^{7}Be line at 477.6 keV by extrapolating from ^{214}Pb peaks at 242, 295, 352, and 480 keV, the ^{226}Ra peak at 186 keV, and the ^{235}U peak at 205 keV. Nuclear yields for these photons are weighted-averages compiled from Delgado et al. (2002) and Morel et al. (2004) for ^{214}Pb and ^{226}Ra, and from Xiaolong and Baosong (2009) for ^{235}U.

Large-volume, close-in counting geometry required for low-level ^{7}Be measurement favors sensitivity at the expense of considerations that complicate efficiency estimates, including (1) increased likelihood of coincidence-summing effects (peak area anomalies caused by failure of the detector to discriminate between independent photon interactions, summing them erroneously) and (2) exacerbated self-absorption of in situ photon emissions, even at relatively high energies such as that of the ^{7}Be photo-emission. Consistent with previous reports (García-Talavera et al., 2001; Yücel et al., 2010), we do not find significant coincident-summing losses from these ^{214}Pb peaks, within the context of our experimental conditions, the precision constraints of standard sources, uncertainties on photon yields, and considering self-attenuation differences between different standard materials. Efficiencies derived from these ^{214}Pb photons are statistically indistinguishable from those derived from a synthetic mixed-nuclide solution (Eckert & Ziegler Isotope Products Laboratories, Valencia, California, USA) in identical geometry and using photopeaks of ^{113}Sn peak at 392 keV, ^{85}Sr at 514 keV, and ^{137}Cs at 662 keV (Fig. 3). Because ^{228}Ac emits photons at many energy levels in rapid cascades, the rate of which exceeds the time-resolution of the detector system, coincidence-summing effects for this nuclide are large and variable from photon to photon (García-Talavera et al., 2001). Efficiencies we observe for the ^{228}Ac 478.3 keV and 911.2 keV photons are up to 10% lower than would be extrapolated from other non-cascading photopeaks, such as those listed above for U-ore standards, and instead must be measured directly using the ^{228}Ac photopeaks themselves in Th-ore standards.

4.2.2. In situ attenuation corrections

Gamma photon attenuation is dependent on the cumulative absorption cross-section of the matrix material, which is a function both of its elemental composition and bulk density. A typical radionuclide calibration solution in 2% HCl (including elemental carrier content and dilute acid matrix) has an absorption cross-section essentially that of liquid water; at 480 keV this is ca. 0.100 cm^2/g or 11.0 cm^2 for 110 g in our adopted 110 cm^3 geometry. By comparison, absorption cross-section for a typical fine-grained sediment is ca. 0.090 cm^2/g, or13.3 cm^2 for 150 g in the same volumetric geometry; this is 17% greater than that of the synthetic standard solution (mass attenuation coefficients drawn from Hubbell and Seltzer, 1996). For a suite of soils and sediments in the same geometry, net efficiency increases from 3.1% to 3.6% as bulk density increases from 0.7 to 1.8 g/cm^3 — a range of 16% relative, far in excess of error expected from any calibration scheme (Fig. 3). Efficiency calibration based on sample bulk density (efficiency vs. density) removes much of these compositional effects (Murray et al., 1987), but use of a direct attenuation measurement collapses internal efficiency uncertainties by an additional factor of 2 or more, to <2% relative, or to the limit either of counting uncertainties or the preparation of homogenous powder standards.

For attenuation corrections we use point-source transmission and a multi-nuclide planar source in a method adapted from Cutshall et al. (1983), by which an in situ attenuation correction, f, is estimated from an *external* transmission measurement at each energy of interest:

$$f = \frac{I/I_0 - 1}{\ln I/I_0}. \tag{5}$$

Here I is the count rate of an emitting source through a sample or standard and I_0 is the count rate through the sample geometry in the absence of any sample, i.e. an empty container. The ratio I/I_0 is conventionally defined as transmission. Net efficiency is measured directly from calibration standards, from which we calculate a "geometric" efficiency term, i.e. efficiency in the absence of attenuation

$$\varepsilon^* = \frac{\varepsilon}{f^*} = \frac{R^*}{A^* \cdot m^* \cdot \gamma \cdot f^* \cdot p} \tag{6}$$

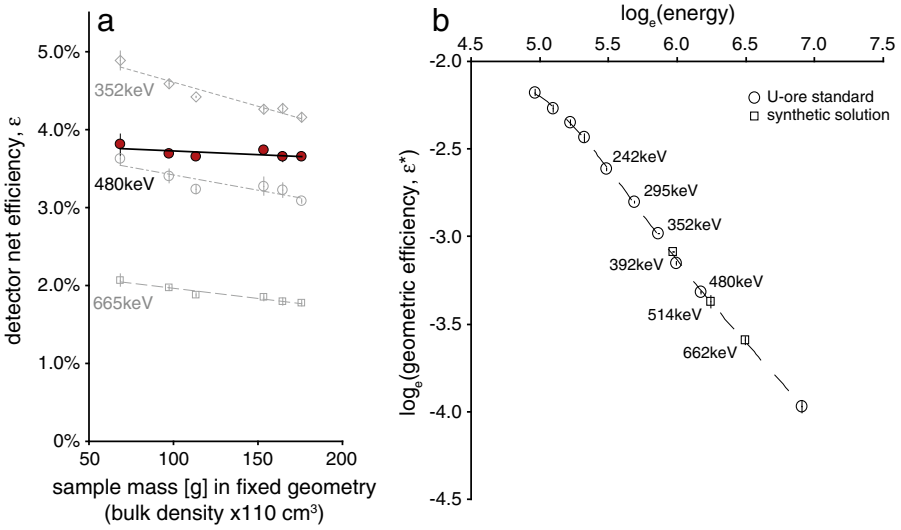

Fig. 3. Efficiency calibration scheme, a: density–efficiency function. In open symbols, net efficiencies at 352, 480, and 665 keV for a range of soil and sediment materials, each spiked ~1% w/w with Uranium ore BL-5 (CCRMP). Density-dependence reflects significant sample self-absorption, even for relatively high-energy gamma photons. Closed circles show geometric efficiency at 480 keV, in which a point-source transmission measurement is used to correct self-absorption effects. b: Energy-efficiency curve in log-scale. Open circles depict U-ore spiked materials, shown with polynomial fit. Squares depict synthetic radionuclide solution, whose absorption cross-section is most similar to organic-rich forest soil. Only by correcting for self-absorption do the two materials provide convergent calibrations in large-volume geometry.

where ε^* is geometric efficiency, ε is net efficiency, R^* is measured count rate of the given photon in the calibration material, A^* is certified activity concentration of the reference ore, m^* is mass of the ore spike, and f^* is measured attenuation correction for the calibration standard. Activity concentration of a nuclide in an unknown sample is then calculated using the geometric efficiency determined from calibration standards as

$$A = \frac{R}{f \cdot \varepsilon^* \cdot \gamma \cdot p \cdot m} \tag{7}$$

where f is attenuation correction measured for each sample. By way of caution, we note that natural ore materials are exceptionally enriched in heavy elements, and increase attenuation of a spiked matrix material at all energies of interest. At 480 keV in Th-ore standards, this amounts to as much as 2% even at conservative spike concentrations. That Larsen and Cutshall (1981) reported no differences between solid and aqueous standard media in their original ^{7}Be methodology is perhaps due to their use of (presumably pure quartz) sand as a representative solid, whereas our sediments typically are enriched in minerals containing heavy elements such as iron and manganese.

4.2.3. Peak shape calibration

Calibration of peak shape parameters (Eq. (3)) requires care. Energy calibration (i.e., energy vs. detector channel number) determines the location of a particular photon centroid, μ, in the gamma spectrum. Accurate centering is particularly important where deconvolution of overlapping peaks is concerned. Most detectors demonstrate a characteristic fine non-linearity in their energy calibration (e.g., Gehrke et al., 1971; Helmer et al., 1971), which also modulates slightly during data collection due to detector gain drift. For this latter reason we characterize the energy calibration in each sample spectrum using large interference-free peaks such as the Pb X-rays at 74 and 78 keV, and gammas of ^{210}Pb at 46 keV, ^{228}Ac at 209 keV, ^{212}Pb at 238 keV, ^{214}Pb at 295 keV, ^{228}Ac at 338 keV, ^{214}Pb at 352 keV, ^{208}Tl at 583 keV, ^{214}Bi at 609 keV, and ^{228}Ac at 911 keV. The centroids of minor peaks such as ^{7}Be may be extrapolated from the function(s) described by centering of these larger peaks. Note that X-ray photopeaks have different shape parameters than those of gamma photons, being both narrower and Lorentzian in shape rather than strictly Gaussian.

Measurement of gamma peak width, σ_G, and especially tailing parameters, requires large peaks that are full-width resolved from baseline (e.g., Valentine et al., 1992; Valentine and Rana, 1996). This is a central challenge to spectra from environmental samples, where nuclide activities are typically low, and count rates and peak areas are consequently small. For this reason we describe σ_G and tailing parameters a priori with calibration materials, and use in situ measure only to confirm our estimates and to screen for cases of gross gain drift or malfunction.

4.3. Methods of analysis

A discussion of analytical methods is crucial, since their selection has consequences for the accuracy and precision of low-level results. The many widely available commercial and freeware gamma software packages all include refined tools for calibration, peak integration and deconvolution. But in our experience software designs necessarily favor universal applicability at the expense of flexibility, and given the various parameters required for deconvolution this can be a liability for the most challenging environmental problems. We follow guidelines given by ANSI N42.14 (1999); the simplest method is preferable, and should allow for careful, visual evaluation of the data reduction process. For the following discussion we adopt generic terminology in describing our experimental methods.

When correcting for significant spectral overlap, the simplest deconvolution method estimates area of the interferent by reference to a large singlet of the same nuclide elsewhere in the spectrum via the ratio of their respective emission yields and measurement efficiencies, i.e. Eq. (1). This of course requires specific knowledge of the interfering nuclide and that the nuclide has multiple emissions lines. The interferent contribution is removed arithmetically by subtraction from the total count rate of the integrated multiplet, e.g. the ^{7}Be + ^{228}Ac duplet, as would be done in the classical total-peak-area (TPA) integration (e.g., Baedecker, 1971). Whereas TPA integration implicitly assumes integration of the entire full-energy singlet, and of each convoluted peak in multiplets, partial-peak-area (PPA) integration has long been recognized as a means of reducing counting uncertainties of small peaks (Sterlinski, 1970; Baedecker, 1971; Kennedy, 1990; Luedeke and Tripard, 1996) by avoiding low signal-to-noise (S/N) peak tails. These gains come at a practical cost, in that PPA requires correction for the integrated partial fraction p, which is calculated as $\sum p_i$ via Eq. (3), of the full-energy peak.

Complete calculation for ^{7}Be activity concentration using digital integration, including the ^{228}Ac correction, may thus be written as

$$A^{\mathrm{Be7}} = \frac{R^{multiplet}_{478\,\mathrm{keV}} - p^{\mathrm{Ac228}}_{478\,\mathrm{keV}} \cdot \frac{R^{\mathrm{Ac228}}_{911\,\mathrm{keV}} \cdot \gamma^{\mathrm{Ac228}}_{478\,\mathrm{keV}} \cdot \varepsilon^{\mathrm{Ac228}}_{478\,\mathrm{keV}}}{p^{\mathrm{Ac228}}_{911\,\mathrm{keV}} \cdot \gamma^{\mathrm{Ac228}}_{911\,\mathrm{keV}} \cdot \varepsilon^{\mathrm{Ac228}}_{911\,\mathrm{keV}}}}{f \cdot \varepsilon^*_{478\,\mathrm{keV}} \cdot \gamma^{\mathrm{Be7}}_{478\,\mathrm{keV}} \cdot p^{\mathrm{Be7}} \cdot m} \cdot \frac{1}{e^{-d\lambda}} \tag{8}$$

where d is time [days] elapsed between reference (sampling) time and mean measurement time, and λ is decay constant (nominally 0.0130 d^{-1}), which together account for analyte decay during the sampling, processing and measurement processes. The nominal cumulative peak integration fraction, p, is properly determined by optimization of statistical uncertainty of the integration; for relatively small peaks this occurs at $\pm 1.4\sigma_G$ (Pauly et al., 1966; DeGeer, 2004; Garcia and Puimedon, 2004). At 478 keV, for 0.5 keV detector channel width, optimal integration width is 2–3 channels, depending on binning effects; for 0.25 keV channel width the optimal number of channels is 6. Expanded uncertainty is readily propagated from Eq. (8) using standard methods (JCGM, 2008).

Least-squares peak fitting (LSQ) is the common alternative to digital integration. There is little consensus regarding universal superiority of one over the other (e.g., Kennedy, 1990). Peak fitting entails optimization of a peak shape model, i.e. Eq. (3), to fit the observed spectrum by routine non-linear least-squares minimization (ANSI, 1999). Peak deconvolution by this method fits multiple peaks simultaneously to describe the observed spectrum, with increasing algorithm complexity required in cases of multiple unknowns and/or uncharacterized background (e.g., Christensen and Heydorn, 1987; Kennedy, 1990; Keyser, 1990; Morháč et al., 1997; Blaauw et al., 1999; Garcia-Talavera and Ulicny, 2003; Morháč and Matoušek, 2009). However, for the present case we have a well-characterized spectrum composed of just two known peaks superimposed on a well-known background; we thus avoid the principal complications of deconvolution (Luo, 2006) and our problem reduces to a simplified effort of parameterizing peak shape models. As our peak shape parameters are predetermined (Section 4.2), the only LSQ solved parameters are peak heights for each peak included in the model. Furthermore, because we have good information on the size of the ^{228}Ac interferent peak, we can constrain the height/area of this peak and solve only for the height of our true unknown: ^{7}Be. Both our PPA and LSQ methods in the ^{7}Be case thus amount to refined "library-oriented" deconvolution methods (Blaauw et al., 1999), truly a best-case scenario in which we bring maximum information to bear on a recalcitrant problem.

To explore the efficacy of the different methods for removing the ^{228}Ac interference from ^{7}Be photopeaks in our experimental samples, below we compare the results from these three deconvolution

methods, TPA, PPA and LSQ, in addition to a TPA method without interference correction ('raw').

5. Experimental results and discussion

5.1. Interferences corrected and bias removed

The effect of environmentally-relevant ^{228}Ac additions on the ^{7}Be photopeak is clear (Fig. 4): with increasing ^{228}Ac activity (note growth in the ^{228}Ac 463 keV peak) the ^{7}Be peak broadens to the high-energy side, reflecting the in-growth of the ^{228}Ac 478.3 keV peak. At the start of our experiment the ^{7}Be peak signal-to-noise (S/N) is ~2.8 and the ^{7}Be:^{228}Ac peak area ratio ranges from 60 to 5 for increasing spike levels. We conclude our experiment when ^{7}Be has decayed to a critical limit of ~0.5 Bq/kg, when S/N is <0.2 and the ^{7}Be:^{228}Ac peak area ratio ranges 1.0 to 0.2 for the different spike levels. In the fifth half-life of measurement we find 2 out of 30 measurements (7%) to be instances of false-negative, a rate consistent with our assessment of detection criteria (see Appendix A). Results for ^{7}Be integration are summarized in Fig. 5, where measurements are presented with decay-correction to a reference time to simplify inter-comparison. But note that with elapsing experimental time the decay correction magnifies absolute uncertainties and exaggerates inaccuracy due to the ^{228}Ac interference (in the case where no correction is applied) or due to bias in the interference correction itself. The sum effect of the decay correction is to sensitize our results to methodological inadequacy, helping to expose any bias that may be present.

Both PPA and LSQ methods give identical variance-weighted average ^{7}Be activities of 12.25 ± 0.30 Bq/kg (mean ± 2SE), which we adopt as our reference ^{7}Be activity concentration. In the unadulterated, natural test material with ample ^{7}Be and typical ^{228}Ac activities, and omitting correction for the ^{228}Ac interference, we measure 11% more ^{7}Be than predicted from our adopted value. This bias exceeds 1σ counting uncertainty, even in these ideal analytical conditions. The absolute error we see is in fact consistent for all 'raw' uncorrected integrations across all spike levels: 13.6 ± 1.2 mBq ^{7}Be per Bq ^{228}Ac (average ± 2SE), near to the nominal 16 mBq we expect (Section 2). Consequently, our 'raw' results among different spike levels demonstrate strong bias — pairwise comparison by Tukey HSD ($F_{4,115}$ = 45.3) gives P<2.2e−16 for the greatest difference, between

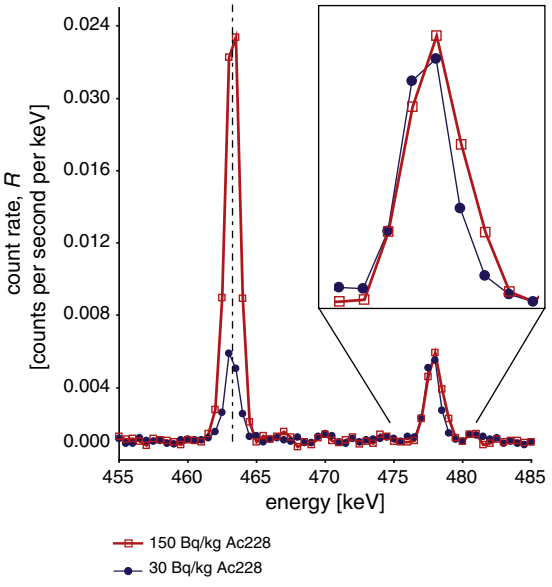

Fig. 4. Additions of ^{232}Th ore to a natural sediment yield visible changes to the ^{7}Be photoregion, notably growth of the ^{232}Th-granddaughter ^{228}Ac 463 keV photopeak and broadening of the ^{7}Be photopeak due to interference via the ^{228}Ac 478.3 keV photopeak.

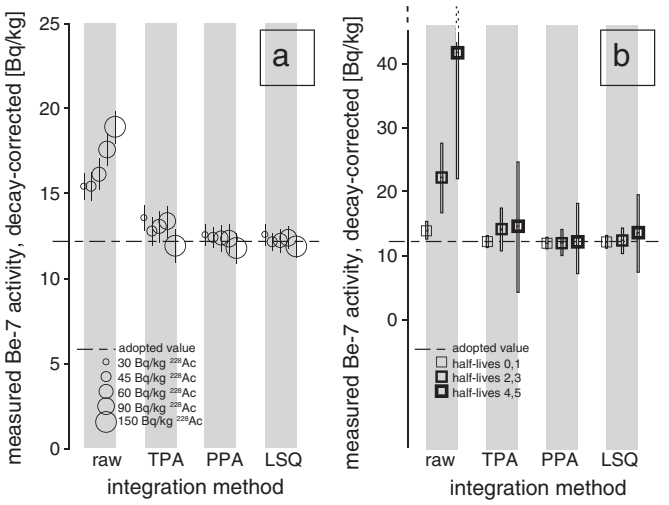

Fig. 5. Comparison of methods for ^{7}Be integration and deconvolution, a: effect of ^{228}Ac spike: variance-weighted ^{7}Be activity (error bars = 2σ SE) for 5 increasing ^{228}Ac spike levels integrated using 4 different methods. TPA method errors are underestimated (see text). Spike levels with PPA and LSQ methods are indistinguishable by Tukey HSD at P> 0.95. b: Effect of decay time and S/N ratio, note y-scale change: arithmetic mean with standard deviation for pooled samples (all spike levels) at intervals of 0–1, 2–3 and 4–5 half-lives for each of 4 integration methods. Decay normalization exaggerates bias, as evident in 'raw' integrations. TPA uncertainty is 2× greater than PPA or LSQ.

the non-spiked and most-highly spiked samples. TPA integration removes much of the bias, but there still are measurable differences among different spike levels ($F_{4,115,2.16}$, P = 0.049). Both PPA and LSQ methods eliminate ^{228}Ac bias, within the statistical limits of our data ($F_{4,115,0.71}$, P = 0.68; $F_{4,115,0.44}$, P = 0.72, respectively). For these latter methods, trending differences in average ^{7}Be activity-concentrations among spike levels are visually suggestive of over-correction, but not statistically significant ($F_{1,3,7.93}$, P = 0.067). This may be an artifact of a relatively low number of total measures, especially at early half-lives.

If real, overcorrection of the ^{228}Ac interference would most likely reflect error in either ^{228}Ac nuclear data, or bias in net efficiency for this photon determined for each of our four detectors. Published uncertainties on yield (7.2% relative) and energy (4% of FWHM) of the ^{228}Ac 478 keV photon are both relatively large, and would propagate errors sensitive to the ^{7}Be:^{228}Ac peak area ratio. Attributing overcorrection to calibration error would require equivalent bias for each of our detectors, as we see no significant differences in ^{7}Be measurement among them ($F_{3,116,0.38}$, P = 0.77). Relative error on the ^{228}Ac efficiency term is ~7%, derived primarily from counting uncertainty on the efficiency calibration, but also uncertainty of the reference Th-ore standard. Direct measure of the ^{228}Ac 478 keV photon efficiency requires cumulative measurements of many days or even weeks to achieve reasonable counting uncertainties. Summing coincidence models (e.g., Yücel et al., 2010) may yield lower uncertainty on this parameter.

5.2. Uncertainty budget and detection limits

Even with our unbiased methods (PPA and LSQ), uncertainties in ^{7}Be measurement are unavoidably high (Table 2). This is simply a reflection of the nuclide's low abundance, the limitation of counting statistics, and the convolution of multiple small peaks. Uncertainties for digital integrations are expanded according to Eq. (8), conforming to counting statistics and peak model parameter uncertainties. Uncertainty estimates for peak areas via least-squares routines are obtained via a linear perturbation method. Evaluation of our uncertainties by the method of Heydorn and Madsen (2005) shows PPA and LSQ methods to be robust yet somewhat conservative ($T_{114,87}$ P = 0.0052

Table 2
Expanded uncertainty for ^{7}Be integration using four experimental conditions *a*, *b*, *c*, and *d*.

	a	*b*	*c*	*d*
Experimental condition				
^{7}Be (Bq/kg)	12	12	1	1
^{228}Ac (Bq/kg)	30	150	30	150
Peak:peak ration	30	6	2.5	0.5
Signal-to-noise	3.0	1.4	0.3	0.1
Expanded ^{7}Be uncertainty				
σ (Bq/kg)	0.6	0.8	0.4	0.6
RSD	5.2%	6.6%	39%	64%
Integration uncertainty[1]				
Parameter	Normalized contribution to total			
R_{Be7}	19.5%	17.7%	45.9%	21.1%
R_{Ac228}	4.3%	8.8%	40.9%	22.9%
p_{Be7}	14.1%	9.8%	0.6%	0.1%
Y_{477keV}	1.1%	0.7%	0.0%	0.0%
m	0.0%	0.0%	0.0%	0.0%
ε_{477keV}	59.9%	41.7%	2.7%	0.6%
Sum contribution	98.8%	78.8%	90.1%	44.8%
Correction uncertainty[2]				
Parameter	Normalized contribution to total			
p_{478keV}	0.1%	1.9%	2.5%	14.4%
$R_{Ac228,91keV}$	0.0%	0.0%	0.2%	0.0%
Y_{478keV}	0.4%	6.5%	2.4%	13.7%
ε_{478keV}	0.7%	11.4%	4.2%	24.1%
p_{911keV}	0.0%	0.0%	0.0%	0.0%
Y_{911keV}	0.0%	0.3%	0.1%	0.6%
ε_{911keV}	0.1%	1.1%	0.4%	2.4%
Sum contribution	1.2%	21.2%	9.9%	55.2%

Contributions to total uncertainty are categorized by their source, either [1]gross peak integration or [2]interference correction for ^{228}Ac, and within each category are attributed to individual calculation parameters as defined in the main text and Eq. (8).

and $P = 0.028$, respectively). These are a factor of 2 improved over theoretical deconvolution precision limits (Terracol et al., 2004) because we are able to provide a priori constraint on the ^{228}Ac peak. Conversely, similarly propagated TPA uncertainties grossly *underestimate* observed variance ($T_{114,158}$ $P = 0.994$). This is likely a result of including additional, untreated interferences, e.g., from peaks at 474 keV and 480 keV (Fig. 1), in the TPA integration of ^{7}Be.

Through analysis of our error budget (Table 2) we confirm that at high ^{7}Be activity and high ^{7}Be:^{228}Ac peak area ratio, uncertainty of the ^{7}Be measure is dominated by Poisson statistics of the duplet integration itself. Background uncertainty is predominant, with a lesser contribution from the ^{7}Be peak itself. Degradation in the measurement due to ^{228}Ac interference is minimal. Nominal external uncertainty is ~6% relative. As ^{7}Be decay proceeds and ^{7}Be:^{228}Ac ratio decreases, uncertainty in the ^{228}Ac correction becomes the dominant source of error. Near detection limits and with significant ^{228}Ac interference, we expect that ^{7}Be uncertainty approaches 70% with even the best integration methods.

6. Conclusions

Given the value of the ^{7}Be tracer and the analytical challenges of low-level work, our principal concern is to reduce ^{7}Be uncertainties to a bare and accurate minimum, since it is the relative abundances of ^{7}Be in samples that informs us of sediment transport pathways, age, source, etc. Total-peak-area (TPA) digital integration can remove much of the ^{228}Ac bias, assuming analysts realize the presence of the ^{228}Ac interferent and background selection limitations. But the TPA method is inherently subject to large, unconstrained uncertainties when integrating small peaks and to bias from multiple spectral features specific to the ^{7}Be photoregion. Both partial-peak area (PPA) digital integrations and least-squares fitting (LSQ) methods improve ^{7}Be precision by up to 50% over conventional TPA integration, if they are carefully calibrated. The PPA method achieves this by trimming channels subject to both the highest degree of interference and highest Poisson uncertainty. Least-squares methods weight constituent peak channels proportionally to their significance, diminishing the influence of peak shoulders and deviations in peak shape as Poisson fluctuations in background and interference increase in influence. Both methods absolutely rely on a priori constraint of the interfering peak to achieve good precision. Allowing the ^{228}Ac peak area to vary as a free parameter in simple least-squares fitting, for example (while retaining its centroid, i.e., its identity) degrades ^{7}Be precision ~40% compared to that of either PPA or constrained LSQ methods, nearly as deficient as the TPA digital method.

All unbiased methods of ^{7}Be quantitation rely on accurate gamma peak models. The effort required to properly calibrate peak shape parameters and both energy- and efficiency-calibration terms is by no means trivial. But this effort need only be expended once in setting up of the low-level gamma spectroscopy laboratory. With widely available means and close evaluation of the environmental gamma spectrum we are able to address risks of false positives, and to produce unbiased and precise ^{7}Be measurements in a variety of natural soils and sediments. The gains in precision we describe here permit the application of the ^{7}Be tracer to new applications (e.g., Hartman, 2010; Hamm, 2011), and should provide better resolving power to those already in use. Example detection limits for ^{7}Be presented here are ~10× improved over those reported 30 years ago by Larsen and Cutshall (1981) for comparable count times and samples sizes, but are by no means the lowest achievable. Because ^{7}Be detection is limited by Compton scattering of gamma emissions derived from the sample itself, Ge crystals and/or ancillary devices that maximize Peak-to-Compton performance (Heusser, 1995; Povinec, 2008) can be used to improve the ^{7}Be MDC. Dual detector Compton-suppression systems, while not without drawbacks, should allow both lower detection limits and improved precision at low ^{7}Be and high ^{228}Ac activities. That previous authors have not reported interfering photopeaks in ^{7}Be measurements is likely attributable to the relative enrichment of their sediment samples in ^{7}Be, their higher instrument background, or perhaps to relatively poor counting efficiency of older gamma detectors.

The known ^{7}Be decay-rate provides a final, well-accepted context for evaluating radionuclide analytical results (Fig. 6), first exploited

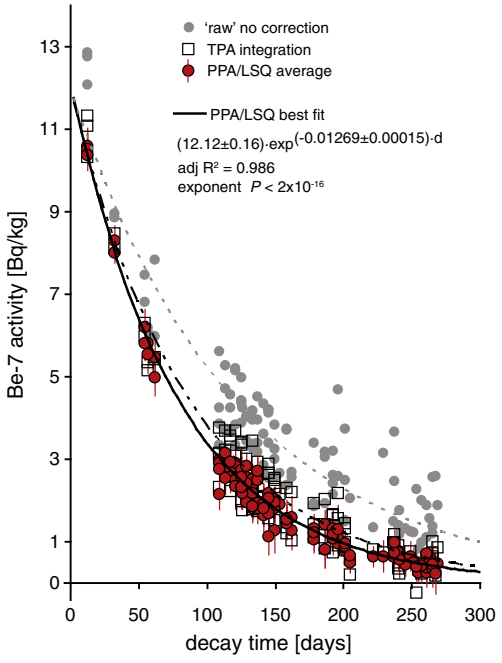

Fig. 6. ^{7}Be decay rate measured by different integration methods yields very different half-lives. For clarity, only the PPA/LSQ averaged data include 1σ error bars. These methods are most precise, unbiased, and yield a decay rate consistent with the accepted value (0.0130^{-d}).

for ^{7}Be gamma spectroscopy by Arnold and Ali Al-Salih (1955) and later by Larsen and Cutshall (1981). Our modern detection efficiencies, numerous measurements, and statistical control allow us to describe the rate of ^{7}Be decay accurately in the most rigorous circumstances, at very low environmental abundances and with significant spectral corrections. Since both PPA and LSQ methods appear to give unbiased results, we average them to reduce integration imprecision — this yields a half-life of 54.62 ± 1.28 d (mean $\pm$ 2SE), just within error of the accepted value of 53.3 d ($F_{1,99,4.53}$, $P = 0.046$). The TPA measure gives 60.8 ± 2.6 d, reflecting pronounced bias in this method, especially at low activities and extended half-lives. The 'raw' uncorrected ^{7}Be decay yields a nonsensical half-life of 88.7 ± 6.4 d. Our best estimate of ^{7}Be decay is somewhat higher than the accepted 53.3 d, the latter being a weighted average derived from a variety of synthetic and metallic beryllium materials (e.g., Norman et al., 2001). Certainly our experimental conditions were not designed to address the ^{7}Be half-life, yet we consider the comparison intriguing in light of variable and longer half-lives reported for ^{7}Be decay related to atomic coordination environment: for Be-oxide, for example, the proposed ^{7}Be half-life is 54.23 ± 0.01 (mean $\pm$ 2SE; Huh, 1999). Indeed, to date, no robust measure has been reported of ^{7}Be decay in an environmentally-derived form.

Appendix A

A.1. Limits of detection, with extension to probabilities of interference

The counting time t required for a given photopeak to emerge above the background continuum is a function of both background count rate and the photopeak count rate, and can be derived from Currie's (1968) empirical critical limit R_C

$$R_C = k_1 \cdot \sqrt{\frac{nR_0}{t}} \tag{A1}$$

where k_1 is the Gaussian fractile for background distribution, n is number of channels in peak, R_0 is background count rate [cps per channel], and t is count time [seconds]. For the samples in our composite spectrum we derive the background count rate, R_0, at 478 keV by linear regression through quiescent background energies. The appropriate criterion for choosing n minimizes the critical limit, and corresponds to $\pm 1.4\sigma_G$ for both detection and integration purposes (Pauly et al., 1966; DeGeer, 2004; Garcia and Puimedon, 2004). A Gaussian fractile k is related to probability of occurrence p_k as

$$p_k = \frac{1}{2}\left[1 - erf\left(\frac{k}{\sqrt{2}}\right)\right]. \tag{A2}$$

For example, in the analysis below we set $k_1 = 1.645$, which encompasses the 2σ (95%) distribution of background observations, and corresponds to a probability of false-positive $\alpha = 5\%$ (ISO, 2000). Corresponding values of the critical count rate R_C for our samples are shown in Fig. 2a — the critical limit declines exponentially with increasing count time with the familiar $(-1/2)$ exponent that defines Poisson phenomena. Longer count times yield better resolving power of peaks from background. Observed peak count rates that exceed R_C are judged to be true photopeaks and not random background fluctuation.

Using Eq. (2), R_C also can be expressed as the activity of ^{228}Ac in a sample that will produce a "detectable" signal at 478.3 keV. In so doing we account for Poisson uncertainty in the photopeak count rate by defining the predicted rate $R_{predict}$ as

$$R_{predict} = R + k_2\sqrt{\frac{R}{t}} \tag{A3}$$

where k_2 is Gaussian fractile for *photopeak* distribution and R is nominal peak count rate obtained via Eq. (2). Here we take $k_2 = 0$, and thus, for a given ^{228}Ac activity, plot the time required for a detectable peak to emerge in *50% of our measurements*. If we then assume that ^{232}Th and ^{228}Ac are in secular equilibrium, we can compare the ^{228}Ac activity in our samples with United Nations (UNSCEAR, 2000) surveys of global ^{232}Th activities. Anticipated count rates at 478.3 keV for global median, low- and high-typical ^{228}Ac activities are plotted as horizontal dashed lines in Fig. 2a.

Finally, by equating the predicted count rate (Eq. (A3)) to the critical threshold count rate (Eq. (A1)), we solve for the counting time required for an interfering peak to emerge above the background continuum with a probability defined by the Gaussian fractile for the photopeak distribution k_2

$$t = \frac{nk_1^2R_0 - 2k_1k_2\sqrt{nRR_0} + k_2^2R}{R^2}. \tag{A4}$$

Eq. (A4) may thus be used to predict the time required for the emergence of the ^{228}Ac 478.3 keV or other peaks with stated probabilities, e.g. 10% ($k_2 = 1.282$) or 1% ($k_2 = 2.326$), as a function of the ^{228}Ac activity. These relations appear in Fig. 2a as solid (50%) or dashed (1% and 10%) curves. Consistent with our composite spectrum, we predict that ^{228}Ac makes significant contributions to routine sample spectra over common count durations. Median global ^{228}Ac activity in soils is detectable at 478 keV with 50% probability in 1.1 days, with 10% probability in 0.6 days, and with 1% probability in 0.3 days. These probabilities represent risks of *Be-7 false positives*, in excess of those we expect due to background phenomena alone.

A.2. Implications for beryllium-7 measurement

The minimum-detectable-activity (MDA) is the lowest a priori activity that we can resolve with stated confidence (ISO, 2000). Expressed per unit mass of sample is MDC, minimum-detectable-activity-concentration. MDC includes uncertainty in the background count rate (Eq. (A1)), which assesses the risk of false-positive via k_1, as well as uncertainty in the photopeak count rate (Eq. (A3)), which assesses the risk of false-negative via k_2. In the case of interference from another photopeak, MDC must include an evaluation of the interferent contribution to background. In this case gross background (R_0) is the sum of continuum and photopeak contributions (Currie, 1968). MDC is calculated similarly as in Eq. (A1) with the addition of the term k_2 to assess uncertainty of the photopeak distribution (Currie, 1968), and transformed into activity concentration (Bq/kg) of the nuclide following Eq. (6):

$$MDC = (k_1 \cdot k_2) \cdot \sqrt{\frac{nR_0}{t}} \cdot (f \cdot \varepsilon^* \cdot \gamma \cdot p \cdot m)^{-1}. \tag{A5}$$

Our results (Fig. 2b) show the anticipated decrease in ^{7}Be MDC with longer count times, but also increasing height of curve with increasing amounts of ^{228}Ac. Because our peaks are small, and our background is high, augmentation of the continuum rather than convolution from the ^{228}Ac 478.3 keV photopeak is primarily responsible for increasing ^{7}Be detection limits — 100% or more in the presence of higher amounts of ^{228}Ac.

References

ANSI, 1999. Use of Germanium spectrometers for the measurement of gamma-ray emission rates of radionuclides, N42.14-1991. National Committee on Radiation Instrumentation. American National Standards Institute, Inc, New York, NY.

Arnold, J.R., Ali Al-Salih, H., 1955. Beryllium-7 produced by cosmic rays. Science 121, 451–453. doi:10.1126/science.121.3144.451.

Baedecker, P.A., 1971. Digital methods of photopeak integration in activation analysis. Analytical Chemistry 43, 405–410. doi:10.1021/ac60298a007.

Blaauw, M., Keyser, R.M., Fazekas, B., 1999. Comparison of alternative methods for multiplet deconvolution in the analysis of gamma-ray spectra. Nuclear Instruments and Methods in Physics Research A 432, 77–89. doi:10.1016/S0168-9002(99)00384-8.

Black, E., Renshaw, C.E., Magilligan, F.J., Kaste, J.M., Dade, W.B., Landis, J.D., 2010. Determining lateral migration rates of meandering rivers using fallout radionuclides. Geomorphol. 123, 364–369. doi:10.1016/j.geomorph.2010.08.004.

Blake, W.H., Wallbrink, P.J., Wilkinson, S.N., Humphreys, G.S., Doerr, S.H., Shakesby, R.A., Tomkins, K.M., 2009. Deriving hillslope sediment budgets in wildfire-affected forests using fallout radionuclide tracers. Geomorphol. 104, 105–116. doi:10.1016/j.geomorph.2008.08.004.

Chabaux, F., Riotte, J., Dequincey, O., 2003. U–Th–Ra fractionation during weathering and river transport. Reviews in Mineralogy and Geochemistry 52, 533–576. doi:10.2113/0520533.

Christensen, L.H., Heydorn, K., 1987. Quality assurance in the determination of overlapping peaks. Journal of Radioanalytical and Nuclear Chemistry 113, 19–34.

Chu, S.Y., Nordberg, H., Firestone, R.B., Ekström, L.P., 1999. Isotope Explorer 2.23. Lawrence Berkeley National Laboratoryhttp://ie.lbl.gov/isoexpl/isoexpl.htm.

Currie, L.A., 1968. Limits for qualitative detection and quantitative determination: application to radiochemistry. Analytical Chemistry 40, 586–593. doi:10.1021/ac60259a007.

Cutshall, N.H., Larsen, I.L., Olsen, C.R., 1983. Direct analysis of 210-Pb in sediment samples: self-absorption correction. Nuclear Instruments and Methods in Physics Research A 206, 309–312. doi:10.1016/0167-5087(83)91273-5.

Dalmasso, J., Maria, H., Hachem, A., Barci, G., Ardisson, G., 1984. High resolution study of the γ-ray spectrum following ^{228}Ac Decay. Journal of Radioanalytical and Nuclear Chemistry 86, 53–62.

Dalmasso, J., Maria, H., Ardisson, G., 1987. ^{228}Th nuclear states fed in ^{228}Ac decay. Physical Review C 36, 2520–2527.

DeGeer, L., 2004. Currie detection limits in gamma-ray spectroscopy. Applied Radiation Isotope 61, 15–160. doi:10.1016/j.apradiso.2004.03.037.

Delgado, J.U., Morel, J., Etcheverry, M., 2002. Measurements of photon emission probabilities from the decay of ^{226}Ra and daughters. Applied Radiation and Isotopes 50, 137–143.

Dibb, J.E., 1989. Atmospheric deposition of Beryllium-7 in the Chesapeake Bay region. Journal of Geophysical Research 94, 2261–2265. doi:10.1029/JD094iD02p02261.

Faye, G.H., Bowman, W.S., Sutarno, R., 1979. CANMET Report 79-4, Uranium Ore BL-5 — A Certified Reference Material. Canada Centre for Mineral and Energy Technology, Natural Resources Canada, Ottawa.

Fisher, G.B., Magilligan, F.J., Kaste, J.M., Nislow, K.H., 2010. Constraining the timescales of sediment sequestration associated with large woody debris using cosmogenic ^{7}Be. Journal of Geophysical Research 115, F01013. doi:10.1029/2009JF001352.

Fitzgerald, S.A., Klump, J.V., Swarzenski, P.W., Mackenzie, R.A., Richards, K.D., 2001. Beryllium-7 as a tracer of short-term sediment deposition and resuspension in the Fox River, Wisconsin. Environmental Science and Technology 35, 300–305.

Garcia, E., Puimedon, J., 2004. Optimal integration window for peak area estimation. Journal of Analytical Atomic Spectrometry 19, 1391–1393. doi:10.1039/b403358b.

García-Talavera, M., Laedermann, J.P., Décombaz, M., Daza, M.J., Quintana, B., 2001. Coincidence summing corrections for the natural decay series in gamma-ray spectrometry. Applied Radiation and Isotopes 54, 769–776.

Garcia-Talavera, M., Ulicny, B., 2003. A genetic algorithm approach for multiplet deconvolution in γ-ray spectra. Nuclear Instruments and Methods in Physics Research Section A 512, 585–594. doi:10.1016/S0168-9002(03)02052-7.

Gascoyne, M., 1992. Geochemistry of the actinides and their daughters, In: Ivanovich, M., Harmon, R.S. (Eds.), Uranium Series Disequilibrium: Applications to Earth, Marine and Environmental Sciences, second ed. Oxford University Press, New York, NY, pp. 34–61.

Gehrke, R.J., Cline, J.E., Heath, R.L., 1971. Determination of relative photopeak efficiency and system linearity of Ge(Li) gamma-ray spectrometers. Nuclear Instruments and Methods in Physics Research 91, 349–356. doi:10.1016/S0029-554X(71)80009-5.

Hamm, N.T., 2011. Experimental Studies of Fine-Particle Transport in Turbulent Flows. Ph.D. dissertation, Department of Earth Science, Dartmouth College, Hanover, New Hampshire, USA.

Hartman, A.D., 2010. Predicting patterns of fluvial erosion using the stream gradient index and short-lived fallout radionuclides. M.S. thesis, Department of Earth Science, Dartmouth College, Hanover, New Hampshire, USA.

Helmer, R.G., Greenwood, R.C., Gehrke, R.J., 1971. Precise comparison and measurement of gamma-ray energies with a Ge(Li) detector. II. 400–1300 keV. Nuclear Instruments Methods 96, 173–196.

Helmer, R.G., 1979. γ-Ray energies for ^{228}Ra–^{228}Ac decay and the ^{228}Th decay chain. Nuclear Instruments and Methods in Physics Research A 164, 355–362.

Heusser, G., 1995. Low-radioactivity background techniques. Annual Review Nuclear Part Science 45, 543–590. doi:10.1146/annurev.ns.45.120195.002551.

Heydorn, K., Madsen, B.S., 2005. Verification of uncertainty budgets. Accreditation and Quality Assurance 10, 403–408. doi:10.1007/s00769-005-0015-6.

Hubbell, J.H., Seltzer, S.M., 1996. Tables of X-ray mass attenuation coefficients and mass energy-absorption coefficients from 1 keV to 20 MeV for elements Z = 1 to 92. NIST. U.S. Department Commercehttp://www.nist.gov/pml/data/xraycoef/index.cfm.

Huh, C.A., 1999. Dependence of the decay rate of Be-7 on chemical forms. Earth and Planetary Science Letters 171, 325–328. doi:10.1016/S0012-821X(99)00164-8.

ISO, 2000. Determination of the Detection Limit and Decision Threshold for Ionizing Radiation Measurements — Part 3: Fundamentals and Application to Counting Measurements by High Resolution Gamma Spectrometry, Without the Influence of Sample Treatment. International Organization for Standardization, Geneva, Switzerland.

JCGM, 2008. Evaluation of measurement data — guide to the expression of uncertainty in measurement. Joint Committee for Guides in Metrology, Bureau International des Poids et Mesures, Sèvres, France.

Kaste, J.M., Norton, S.A., Hess, C.T., 2002. Environmental chemistry of Beryllium-7. Reviews in Mineralogy and Geochemistry 50, 271–289. doi:10.2138/rmg.2002.50.6.

Kaste, J.M., Bostick, B.C., Heimsath, A.M., Steinnes, E., Friedland, A.J., 2011. Using atmospheric fallout to date organic horizon layers and quantify metal dynamics during decomposition. Geochimica et Cosmochimica Acta 75, 1642–1661. doi:10.1016/j.gca.2011.01.011.

Kennedy, G., 1990. Comparison of photopeak integration methods. Nuclear Instruments and Methods in Physics Research Section A 299, 349–353. doi:10.1016/0168-9002(90)90804-F.

Keyser, R.M., 1990. Deconvolution of gamma-ray peak doublets as a function of peak separation and relative amplitude. Nuclear Instruments and Methods in Physics Research Section A 286, 403–408. doi:10.1016/0168-9002(90)90887-C.

Larsen, I.L., Cutshall, N.H., 1981. Direct determination of ^{7}Be in sediments. Earth and Planetary Science Letters 54, 379–384. doi:10.1016/0012-821X(81)90053-4.

Luedeke, T.P., Tripard, G.E., 1996. A channel-by-channel method of reducing the errors associated with peak area integration. Nuclear Instruments and Methods in Physics Research Section A 372, 283–288. doi:10.1016/0168-9002(95)01298-2.

Luo, L., 2006. Chemometrics and its application to X-ray spectrometry. X-ray Spectrometry 35, 215–225. doi:10.1002/xrs.

Matisoff, G., Wilson, C.G., Whiting, P.J., 2005. The 7Be/210Pbxs ratio as an indicator of suspended sediment age or fraction new sediment in suspension. Earth Surface Processes and Landforms 30, 1191–1201. doi:10.1002/esp. 1270.

Morháč, M., Kliman, J., Matoušek, V., Veselsky, M., Turzo, I., 1997. Efficient one- and two-dimensional Gold deconvolution and its application to γ-ray spectra decomposition. Nuclear Instruments and Methods in Physics Research Section A 401, 385–408. doi:10.1016/S0168-9002(97)01058-9.

Morháč, M., Matoušek, V., 2009. Complete positive deconvolution of spectrometric data. Digital Signal Processing 19, 372–392. doi:10.1016/j.dsp. 2008.06.002.

Morel, J., Sepman, S., Rasko, M., Terechtchenko, E., Delgado, J.U., 2004. Precise determination of photon emission probabilities for the main X- and γ-rays of ^{226}Ra in equilibrium with daughters. Applied Radiation and Isotopes 60, 341–346. doi:10.1016/j.apradiso.2003.11.038.

Murray, A.S., Marten, R., Johnston, A., Martin, P., 1987. Analysis for naturally occurring radionuclides at environmental concentrations by gamma spectrometry. Journal of Radioanalytical and Nuclear Chemistry 115, 263–288. doi:10.1007/BF02037443.

Nagai, H., Tada, W., Matsumura, H., Aze, T., Noguchi, M., Matsuzaki, H., 2004. Measurement of 7Be at MALT. Nuclear Instruments and Methods in Physics Research Section B 223–224, 237–241. doi:10.1016/S0168-583X(00)00124-5.

Norman, E.B., Rech, G.A., Browne, E., Larimer, R.-M., Dragowsky, M.R., Chan, Y.D., Isaac, M.C.P., McDonald, R.J., Smith, A.R., 2001. Influence of physical and chemical environments on the decay rates of ^{7}Be and ^{40}K. Physics Letters B 519, 15–22. doi:10.1016/S0370-2693(01)01097-8.

Oddone, M., Giordani, L., Giacobbo, F., Mariani, M., Morandi, S., 2008. Practical considerations regarding high resolution gamma-spectrometry measurements of naturally occurring radioactive samples. Journal of Radioanalytical and Nuclear Chemistry 277, 579–585. doi:10.1007/s10967-007-7113-3.

Olsen, C.R., Larsen, I.L., Lowry, P.D., Cutshall, N.H., 1986. Geochemistry and deposition of ^{7}Be in river-estuarine and coastal waters. Journal of Geophysical Research 91, 896–908. doi:10.1029/JC091iC01p00896.

Pauly, J., Guzzi, G., Girardi, F., Borella, A., 1966. Application of gamma ray spectrometry and computer techniques to the determination of the minimum detectable content of trace elements in neutron activated materials. Nuclear Instruments and Methods 42, 15–25. doi:10.1016/0029-554X(66)90262-X.

Povinec, P.P., 2008. Low-level gamma-ray spectrometry for environmental samples. Journal of Radioanalytical and Nuclear Chemistry 276, 771–777. doi:10.1007/s10967-008-0631-9.

Raisbeck, G.M., Yiou, F., 1988. Measurement of ^{7}Be by accelerator mass spectrometry. Earth and Planetary Science Letters 89, 103–108. doi:10.1016/0012-821X(88)90035-0.

Saari, H., Schmidt, S., Castaing, P., Blanc, G., Sautour, B., Masson, O., Cochran, J.K., 2010. The particulate ^{7}Be/^{210}Pb$_{xs}$ and ^{234}Th/^{210}Pb$_{xs}$ activity ratios as tracers for tidal-to-seasonal particle dynamics in the Gironde estuary (France): implications for the budget of particle-associated contaminants. Science of the Total Environment 408, 4784–4794. doi:10.1016/j.scitotenv.2010.07.017.

Salant, N.S., Renshaw, C.E., Magilligan, F.J., Kaste, J.M., Nislow, K.H., Heimsath, A.M., 2006. The use of short-lived radionuclides to quantify transitional bed material transport in a regulated river. Earth Surface Processes and Landforms 32, 509–524. doi:10.1002/esp.

Schuller, P., Walling, D.E., Iroume, A., Castillo, A., 2010. Use of Beryllium-7 to study the effectiveness of woody trash barriers in reducing sediment delivery to streams after forest clearcutting. Soil Tillage Research 110, 143–153. doi:10.1016/j.still.2010.07.004.

Smith, C.W., Steger, H.F., Bowman, W.S., 1986. The certification of Thorium and Uranium concentrations in CCRMP reference material OKA-2. CANMET Mineral Sciences Laboratories Division Report MSL 86–154. Natural Resources Canada, Ottawa, Canada.

Sterlinski, S., 1970. Features of the modified Covell method for computation of total absorption peak areas in complex gamma-ray spectra. Analytical Chemistry 42, 151–155. doi:10.1021/ac60284a017.

Terracol, S.F., Ali, S., Nierdermayr, T.R., Hau, I.D., Drury, O.B., Ali, Z.A., Miyazaki, T., Cunningham, M.F., Dreyer, J.G., Leacock, J.D., Friedrich, S., 2004. Ultra-high resolution gamma-ray spectrometer development for nuclear attribution and non-proliferation applications. IEEE Nuclear Science Symposium Conference Rec. 2, 1006–1013. doi:10.1109/NSSMIC.2004.1462376.

Todd, J.F., Wong, G.T.F., Olsen, C.R., Larsen, I.L., 1989. Atmospheric depositional characteristics of Beryllium-7 and Lead-210 along the southeastern Virginia coast. Journal of Geophysical Research 84 (D8), 11,106–11,116. doi:10.1029/JD094iD08p11106.

UNSCEAR, 2000. United Nations Scientific Committee on the Effects of Atomic Radiation, Volume 1: Sources and Effects of Ionizing Radiation, Annex B: Exposures from Natural Radiation Sources, Vienna, Austria.

Valentine, J.D., Fleming, R.F., Wehe, D.K., Knoll, G.F., 1992. Uncertainty of centroid and full-width at half maximum determinations and the effect of binning data. Nucl. Sci. Symp. Med. Imag. Conf. 1992, Orlando, FL — Conference Record of the 1992 IEEE. doi:10.1109/NSSMIC.1992.301175.

Valentine, J.D., Rana, A.E., 1996. Centroid and full-width at half maximum uncertainties of histogrammed data with an underlying Gaussian distribution — the moments method. IEEE Transactions on Nuclear Science 43, 2501–2508. doi:10.1109/23.539399.

Wallbrink, P.J., Murray, A.S., 1993. The use of fallout nuclides as indicators of erosion processes. Journal Hydrology Processes 7, 297–304. doi:10.1002/hyp. 3360070307.

Wallbrink, P.J., Murray, A.S., 1994. Fallout of Be-7 in South Eastern Australia. Journal of Environmental Radioactivity 25 (3), 213–218. doi:10.1016/0265-931X(94)90074-4.

Walling, D.E., Woodward, J.C., 1992. Use of radiometric fingerprints to derive information on suspended sediment sources. Erosion and Sediment Transport Monitoring Programmes in River Basins: International Association of Hydrological Scientists Publication, 210, pp. 153–164.

Walling, D.E., Schuller, P., Zhang, Y., Iroume, A., 2009. Extending the timescale for using Beryllium-7 measurements to document soil redistribution by erosion. Water Resources Research 45 (2), 1–13. doi:10.1029/2008WR007143.

Whiting, P.J., Matisoff, G., Fornes, W., Soster, F.M., 2005. Suspended sediment sources and transport distances in the Yellowstone River basin. GSA Bulletin 117 (3–4), 515–529. doi:10.1130/B25623.1.

Wilson, C.G., Matisoff, G., Whiting, P.J., 2003. Short-term erosion rates from a ^{7}Be inventory balance. Earth Surface Processes and Landforms 28, 967–977. doi:10.1002/esp. 509.

Yücel, H., Solmaz, A.N., Kose, E., Bor, D., 2010. A semi-empirical method for calculation of true coincidence corrections for the case of a close-in detection in gamma-ray spectrometry. Journal of Radioanalytical and Nuclear Chemistry 283, 305–312. doi:10.1007/s10967-009-0360-8.

Xiaolong, H., Baosong, W., 2009. Evaluation of ^{235}U decay data. Applied Radiation and Isotopes 67, 1541–1549. doi:10.1007/s10967-009-0360-8.

Zhu, J., Olsen, C.R., 2009. Beryllium-7 atmospheric deposition and sediment inventories in the Neponset River estuary, Massachusetts, USA. Journal of Environmental Radioactivity 100, 192–197. doi:10.1016/j.jenvrad.2008.11.013.